CrossMark

ORIGINAL PAPER

B. Herrmann-Priesnitz · **W. R. Calderón-Muñoz** · **R. Soto**

Stability and receptivity of boundary layers in a swirl flow channel

Abstract The analysis of the disturbances on a spiraling base flow is relevant for the design, operation, and control of technological devices such as parallel-disk turbines and swirl flow channel heat sinks. Spiraling inflow inside an annular cavity closed at the top and bottom is analyzed in the framework of modal and nonmodal stability theories. Local and parallel flow approximations are applied, and the inhomogeneous direction is discretized using the Chebyshev collocation method. The optimal growth of initial disturbances and the optimal response to external harmonic forcing are characterized by the exponential and the resolvent of the dynamics matrix. As opposed to plane Poiseuille flow, transient growth is small, and consequently, it does not play a role in the transition mechanism. The transition is attributed to a crossflow instability that occurs because of the change in the shape of the velocity profile due to rotational effects. Agreement is found between the critical Reynolds number predicted in this work and the deviation of laminar behavior observed in the experiments conducted by Ruiz and Carey (J Heat Transfer 137(7):071702, 2015). For the harmonically driven problem, an energy amplification of $O(100)$ is observed for spiral crossflow waves. Transition to turbulence should be avoided to ensure the safe operation of a parallel-disk turbine, whereas large forcing amplification may be sought to promote mixing in a swirl flow channel heat sink. The analysis presented predicts and provides insight into the transition mechanisms. Due to its easy implementation and low computational cost, it is particularly useful for the early stages of engineering design.

1 Introduction

The spiraling inflow inside an annular cavity closed at the top and bottom has recently regained interest for its relevance to applications in turbomachinery and high heat flux dissipation systems. Scaling of parallel-disk turbines for uses in the microscale has been investigated by Krishnan et al., Pfenniger et al., and Sengupta and Guha among others [7,12,19]. Ruiz and Carey proposed a novel swirl flow microchannel heat sink for high heat flux applications such as cooling electronics and concentrated solar photovoltaics [14]. In subsequent work, a dye injection experiment revealed a considerable increase in dye diffusion when the flow rate going through the channel exceeded 190 ml/min. In the same work, the authors also observed that, for flow rates over

B. Herrmann-Priesnitz (✉) · W. R. Calderón-Muñoz
Department of Mechanical Engineering, FCFM, Universidad de Chile, Beauchef 851, Santiago, Chile
E-mail: bherrman@ing.uchile.cl

W. R. Calderón-Muñoz
Energy Center, FCFM, Universidad de Chile, Av. Tupper 2007, Santiago, Chile
E-mail: wicalder@ing.uchile.cl

R. Soto
Physics Department, FCFM, Universidad de Chile, Av. Blanco Encalada 2008, Santiago, Chile
E-mail: rsoto@dfi.uchile.cl

190 ml/min, laminar theory significantly underpredicted their experimental measurements for pressure drop and total heat flux, and they attributed these results to hydrodynamic instabilities [15].

Steady-state flow was studied numerically using integral methods by Herrmann-Priesnitz et al. [4], and different boundary layer structures were observed depending on the governing parameters. Parabolic velocity profiles are found for low Reynolds numbers, while large inflection of the radial velocity component occurs for higher values. Whether these highly inflected profiles can occur in a real world device is a matter of stability. Stability and receptivity analyses are also motivated by its relevance to design, operation, and control of the parallel-disk turbine and the swirl flow channel heat sink.

Velocity profiles found in this type of channel are similar to those observed in other rotating boundary layer flows, such as von Kármán and Bödewadt flows. The first experimental observation of stationary crossflow vortices and the first theoretical stability analysis for the rotating disk flow were presented by Gregory et al. [2]. Work on the modal and spatial stability continued with Malik, who computed the neutral curves for stationary disturbances using the parallel flow approximation [10]. Lingwood followed by studying the absolute or convective nature of the instabilities [8]. More recently, Serre et al. and Lopez et al. used DNS and found that the Bödewadt layer is unstable to axisymmetric circular radial waves and three-dimensional multi-armed spiral waves [9,20]. In a follow-up study, Do et al. [1] showed that in the absence of any external forcing, the circular waves are transitory, but low amplitude forcing can sustain them indefinitely.

Over the past two decades, nonmodal stability theory has emerged to provide a more complete picture of the linear perturbation dynamics for fluid flows using an initial-value problem formulation [16–18]. The modal approach characterizes a flow as stable if all the eigenvalues of the dynamics operator are located on the left half of the complex plane. Nevertheless, for eigenvalues with negative real part, the flow may experience a large amplification due to linear transient growth before decaying asymptotically [21]. The formulation as an initial-value problem allows the incorporation of an external harmonic forcing term that may represent free-stream turbulence, wall roughness, acoustic perturbations, or body forces among others. The response of the system to these external disturbances, i.e., receptivity of the flow, is determined by the particular solution to the harmonically driven problem. Neither modal nor nonmodal stability and receptivity analyses for the swirl flow channel have been reported elsewhere.

In this study, the formulation of a linear initial-value problem for the perturbation dynamics in a swirl flow channel is detailed. The methodology to apply the local and parallel flow approximations based on order of magnitude arguments is presented. We calculate the optimal energy growth of initial disturbances, and we examine the dependence of the maximum growth on the wavenumbers. We also calculate the optimal response to external harmonic forcing and examine its dependence on the wavenumbers. Unlike in plane Poiseuille flow, rather than transient energy growth of disturbances, the transition to turbulence is attributed to the change from parabolic to inflected base flow velocity profiles due to rotational effects when increasing the Reynolds number.

2 Governing equations

2.1 The base flow

The swirl flow channel consists of an annular cavity, which is open at the outer and inner radii, r_o and r_i, the top and bottom boundaries are solid walls with a separation of $2h$, and it has a very small aspect ratio $h/r_o \ll 1$. Incompressible fluid enters the channel at r_o at an inlet angle θ_o with respect to the tangent, spirals radially inward, and exits through r_i. A schematic of the swirl flow channel as well as the cylindrical system of coordinates used is shown in Fig. 1a. Steady-state flow is axisymmetric and presents a boundary layer nature, and it is therefore governed by

$$\frac{1}{r}\frac{\partial (rU)}{\partial r} + \frac{\partial W}{\partial z} = 0, \tag{1a}$$

$$U\frac{\partial U}{\partial r} + W\frac{\partial U}{\partial z} - \frac{V^2}{r} = -\frac{1}{\rho}\frac{\partial P}{\partial r} + \nu\frac{\partial^2 U}{\partial z^2}, \tag{1b}$$

$$U\frac{\partial V}{\partial r} + W\frac{\partial V}{\partial z} + \frac{UV}{r} = \nu\frac{\partial^2 V}{\partial z^2}, \tag{1c}$$

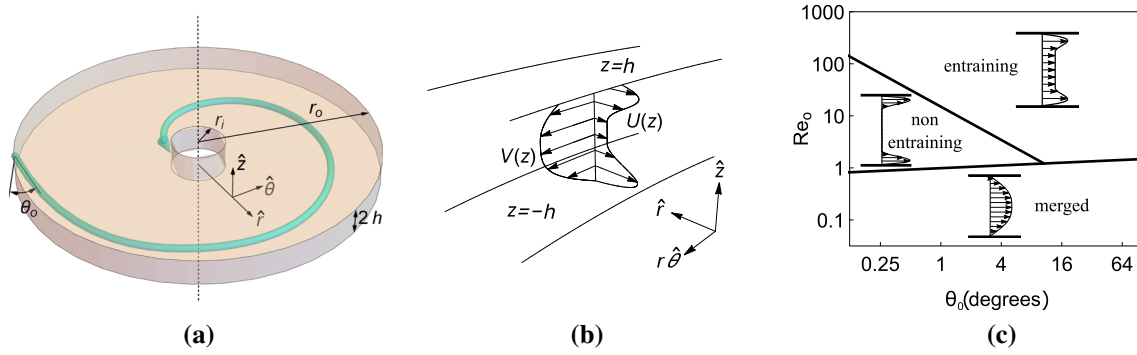$$0 = -\frac{1}{\rho}\frac{\partial P}{\partial z}, \tag{1d}$$

Fig. 1 a Schematic of the swirl flow channel and cylindrical system of coordinates. **b** Base flow schematic and local system of coordinates. **c** Classification of the steady-state boundary layer structures on the Re_o–θ_o space in log scale, based on the radial velocity profiles [5]

$$\mathbf{U} = 0 \text{ at } z = \pm h, \quad \mathbf{U} = U_o \left(1, \cot(\theta_o), 0\right)^{\mathrm{T}} \text{ at } r = r_o, \quad P = 0 \text{ at } r = r_i, \tag{1e}$$

where $\mathbf{U} = (U, V, W)^{\mathrm{T}}$ is the steady-state velocity field in cylindrical coordinates $(\hat{\mathbf{r}}, \hat{\theta}, \hat{\mathbf{z}})$, P is the steady-state pressure, and ρ and ν are the density and kinematic viscosity. Boundary conditions are shown in Eq. (1e): no-slip at the channel walls, velocity $U_o \left(1, \cot(\theta_o), 0\right)^{\mathrm{T}}$ at the inlet, and a reference pressure is set at the outlet. The parameters governing the steady-state flow are the inlet angle θ_o and a flow rate Reynolds number defined as $Re_o = U_o h^2/(\nu r_o)$. The solution to Eqs. (1) is approximated using the method developed in Ref. [4], which considers the formulation of a flow model for the mass and momentum transfer coupled between viscous boundary layers and an inviscid core region. The resulting equations are solved using an integral method and a space-marching technique, and the main advantage of this method is the low computational cost that allows fast exploration of the parameter space [4,5]. Rotation of the fluid induces a crossflow and entrainment of fluid toward the channel walls; therefore, three different boundary layer structures may develop depending on the flow rate Reynolds number and the flow inlet angle: merged, entraining, or nonentraining. These structures are classified based on the shape of the radial velocity profile, as shown in Fig. 1c.

2.2 Linearized perturbation equations

In this section, we cover in detail the formulation of the stability and receptivity problems for the swirl flow channel. The approximations presented allow these problems to be solved using standard nonmodal techniques taken from, e.g., Schmid and Henningson [18].

Linearizing the incompressible Navier–Stokes equations in cylindrical coordinates about an axisymmetric base flow yields the following system of equations:

$$\frac{\partial u}{\partial r} + \left(\frac{u}{r}\right)_c + \frac{1}{r}\frac{\partial v}{\partial \theta} + \frac{\partial w}{\partial z} = 0, \tag{2a}$$

$$\frac{\partial u}{\partial t} + U\frac{\partial u}{\partial r} + \frac{V}{r}\frac{\partial u}{\partial \theta} + w\frac{\partial U}{\partial z} + \left(u\frac{\partial U}{\partial r} + W\frac{\partial u}{\partial z}\right)_{\mathrm{np}} - \left(\frac{2Vv}{r}\right)_c$$
$$= -\frac{\partial p}{\partial r} + \frac{1}{Re}\left[\frac{\partial^2 u}{\partial r^2} + \frac{1}{r^2}\frac{\partial^2 u}{\partial \theta^2} + \frac{\partial^2 u}{\partial z^2} + \left(\frac{1}{r}\frac{\partial u}{\partial r} - \frac{u}{r^2} - \frac{2}{r^2}\frac{\partial v}{\partial \theta}\right)_c\right] + f_u, \tag{2b}$$

$$\frac{\partial v}{\partial t} + U\frac{\partial v}{\partial r} + \frac{V}{r}\frac{\partial v}{\partial \theta} + w\frac{\partial V}{\partial z} + \left(u\frac{\partial V}{\partial r} + W\frac{\partial v}{\partial z}\right)_{\mathrm{np}} + \left(\frac{uV + Uv}{r}\right)_c$$
$$= -\frac{1}{r}\frac{\partial p}{\partial \theta} + \frac{1}{Re}\left[\frac{\partial^2 v}{\partial r^2} + \frac{1}{r^2}\frac{\partial^2 v}{\partial \theta^2} + \frac{\partial^2 v}{\partial z^2} + \left(\frac{1}{r}\frac{\partial v}{\partial r} - \frac{v}{r^2} + \frac{2}{r^2}\frac{\partial u}{\partial \theta}\right)_c\right] + f_v, \tag{2c}$$

$$\frac{\partial w}{\partial t} + U\frac{\partial w}{\partial r} + \frac{V}{r}\frac{\partial w}{\partial \theta} + \left(u\frac{\partial W}{\partial r} + w\frac{\partial W}{\partial z} + W\frac{\partial w}{\partial z}\right)_{\mathrm{np}}$$
$$= -\frac{\partial p}{\partial z} + \frac{1}{Re}\left[\frac{\partial^2 w}{\partial r^2} + \frac{1}{r^2}\frac{\partial^2 w}{\partial \theta^2} + \frac{\partial^2 w}{\partial z^2} + \left(\frac{1}{r}\frac{\partial w}{\partial r}\right)_c\right] + f_w, \tag{2d}$$

where $\mathbf{u} = (u, v, w)^{\mathrm{T}}$ is the perturbation velocity and p is the perturbation pressure. We have added an external forcing term $(f_u, f_v, f_w)^{\mathrm{T}}$ to the momentum equations, which will later be used for the receptivity analysis. The terms inside the parentheses $(\;)_{\mathrm{c}}$ and $(\;)_{\mathrm{np}}$ correspond to curvature and nonparallel flow effects, respectively. Equations (2) have been nondimensionalized using the half-height of the channel, h, as the characteristic length scale, and the velocity magnitude $\sqrt{U^2 + V^2}$ at the midplane of the channel as the characteristic velocity scale.

In this study, we are concerned with the local behavior of flow structures of length scale h, around a certain radial station r. If the radius is sufficiently large compared to the length scales of interest, i.e., $\varepsilon = h/r \ll 1$, the flow can be regarded as locally Cartesian in the coordinates $(\hat{\mathbf{r}}, r\hat{\theta}, \hat{\mathbf{z}})$; therefore, the curvature terms $(\;)_{\mathrm{c}}$ can be neglected. Due to the boundary layer nature of the flow, the normal velocity component is much smaller than those parallel to the walls, i.e., $W \ll U, V$, and the velocity gradient in the radial direction is much smaller than the gradient normal to wall, i.e., $\partial U/\partial r, \partial V/\partial r \ll \partial U/\partial z, \partial V/\partial z$. In fact, these are smaller by a factor of order $O(\varepsilon)$, and by neglecting them, we get $\mathbf{U} \approx (U(z), V(z), 0)^{\mathrm{T}}$. This results in the elimination of the nonparallel flow effects denoted by $(\;)_{\mathrm{np}}$, which is known in the literature as the parallel flow approximation. Both, the local system of coordinates and a schematic of the parallel base flow are shown in Fig. 1b.

Using the local base flow $(U(z), V(z), 0)^{\mathrm{T}}$ and the parallel flow approximation yields the following system of equations:

$$\frac{\partial u}{\partial r} + \frac{1}{r}\frac{\partial v}{\partial \theta} + \frac{\partial w}{\partial z} = 0, \tag{3a}$$

$$\frac{\partial u}{\partial t} + U\frac{\partial u}{\partial r} + \frac{V}{r}\frac{\partial u}{\partial \theta} + wU' = -\frac{\partial p}{\partial r} + \frac{1}{Re}\left(\frac{\partial^2 u}{\partial r^2} + \frac{1}{r^2}\frac{\partial^2 u}{\partial \theta^2} + \frac{\partial^2 u}{\partial z^2}\right) + f_u, \tag{3b}$$

$$\frac{\partial v}{\partial t} + U\frac{\partial v}{\partial r} + \frac{V}{r}\frac{\partial v}{\partial \theta} + wV' = -\frac{1}{r}\frac{\partial p}{\partial \theta} + \frac{1}{Re}\left(\frac{\partial^2 v}{\partial r^2} + \frac{1}{r^2}\frac{\partial^2 v}{\partial \theta^2} + \frac{\partial^2 v}{\partial z^2}\right) + f_v, \tag{3c}$$

$$\frac{\partial w}{\partial t} + U\frac{\partial w}{\partial r} + \frac{V}{r}\frac{\partial w}{\partial \theta} = -\frac{\partial p}{\partial z} + \frac{1}{Re}\left(\frac{\partial^2 w}{\partial r^2} + \frac{1}{r^2}\frac{\partial^2 w}{\partial \theta^2} + \frac{\partial^2 w}{\partial z^2}\right) + f_w, \tag{3d}$$

where $'$ denotes differentiation of the base flow with respect to z. The local temporal evolution problem for the perturbations is completed with appropriate initial conditions and no-slip boundary conditions on the channel walls, i.e., $u = v = w = 0$ at $z = \pm 1$. Equations (3) have coefficients that do not depend on r and θ, and this allows for the perturbation variables to be expanded as Fourier modes in these directions as $\mathbf{u}(r, \theta, z, t) = \hat{\mathbf{u}}(z, t)\,\mathrm{e}^{\mathrm{i}(\alpha r + m\theta)}$, where α is the radial wavenumber and m is the integer azimuthal wavenumber. Identical expansions are carried out for the perturbation pressure and external forcing terms. The governing equations are simplified to

$$\mathrm{i}\alpha\hat{u} + \mathrm{i}\beta\hat{v} + \mathcal{D}\hat{w} = 0, \tag{4a}$$

$$\frac{\partial\hat{u}}{\partial t} + \mathrm{i}\left(\alpha U + \beta V\right)\hat{u} + U'\hat{w} = -\mathrm{i}\alpha\hat{p} + \frac{1}{Re}\left(\mathcal{D}^2 - k^2\right)\hat{u} + \hat{f}_u, \tag{4b}$$

$$\frac{\partial\hat{v}}{\partial t} + \mathrm{i}\left(\alpha U + \beta V\right)\hat{v} + V'\hat{w} = -\mathrm{i}\beta\hat{p} + \frac{1}{Re}\left(\mathcal{D}^2 - k^2\right)\hat{v} + \hat{f}_v, \tag{4c}$$

$$\frac{\partial\hat{w}}{\partial t} + \mathrm{i}\left(\alpha U + \beta V\right)\hat{w} = -\mathcal{D}\hat{p} + \frac{1}{Re}\left(\mathcal{D}^2 - k^2\right)\hat{w} + \hat{f}_w, \tag{4d}$$

where $\beta = m/r$, the total wavenumber is $k = (\alpha^2 + \beta^2)^{\frac{1}{2}}$, and $\mathcal{D}$ denotes differentiation with respect to z of the perturbation variables. We want to rewrite the system in terms of the normal vorticity $\hat{\eta}$ and the normal velocity $\hat{w}$ instead of the primitive variables. To do this, we first derive the transport equation for $\hat{\eta}$ by taking the z component of the curl of the momentum equations (4b)–(4d). Secondly, we obtain an expression for the pressure by taking the divergence of the momentum equations (4b)–(4d) and using the continuity equation (4a). Substituting the resulting expression into Eq. (4d), we eliminate $\hat{p}$ from the system and get

$$\mathcal{M}\frac{\partial\hat{w}}{\partial t} + \mathrm{i}\mathcal{M}\left(\alpha U + \beta V\right)\hat{w} + \mathrm{i}\left(\alpha U'' + \beta V''\right)\hat{w} + \frac{1}{Re}\mathcal{M}^2\hat{w} = \mathrm{i}\alpha\mathcal{D}\hat{f}_u + \mathrm{i}\beta\mathcal{D}\hat{f}_v + k^2\hat{f}_w, \tag{5a}$$

$$\frac{\partial\hat{\eta}}{\partial t} + \mathrm{i}\left(\alpha U + \beta V\right)\hat{\eta} + \frac{1}{Re}\mathcal{M}\hat{\eta} = \mathrm{i}\left(\alpha V' - \beta U'\right)\hat{w} + \mathrm{i}\beta\hat{f}_u - \mathrm{i}\alpha\hat{f}_v, \tag{5b}$$

where $\mathcal{M} = (k^2 - \mathcal{D}^2)$. The no-slip boundary conditions for the normal vorticity and normal velocity become $\mathcal{D}\hat{w}(\pm 1) = \hat{w}(\pm 1) = \hat{\eta}(\pm 1) = 0$. Equations (5) are discretized using the Chebyshev collocation method, and the operator $\mathcal{D}$ is replaced with the Chebyshev differentiation matrix $\mathbf{D}$. We obtain a linear dynamical system where the state variables are the normal velocity and normal vorticity evaluated at the collocation points. The matrix representation of the system is

$$\frac{\mathrm{d}}{\mathrm{d}t}\begin{bmatrix} \hat{w} \\ \hat{\eta} \end{bmatrix} = \underbrace{\begin{bmatrix} \mathbf{L_{OS}} & 0 \\ \mathbf{L_C} & \mathbf{L_{SQ}} \end{bmatrix}}_{\mathbf{L}}\begin{bmatrix} \hat{w} \\ \hat{\eta} \end{bmatrix} + \underbrace{\begin{bmatrix} i\alpha\mathbf{M}^{-1}\mathbf{D} & i\beta\mathbf{M}^{-1}\mathbf{D} & \mathbf{M}^{-1}k^2 \\ i\beta & -i\alpha & 0 \end{bmatrix}}_{\mathbf{B}}\begin{bmatrix} \hat{f}_u \\ \hat{f}_v \\ \hat{f}_w \end{bmatrix}, \tag{6}$$

where $\mathbf{L_{OS}}$, $\mathbf{L_{SQ}}$, and $\mathbf{L_C}$ are the familiar Orr-Sommerfeld, Squire, and coupling operators for a base flow that has velocity components along both, the spanwise and streamwise, directions. The rate of change of the state vector $\hat{\mathbf{q}} = (\hat{w}, \hat{\eta})^\mathrm{T}$ is related to its current state by operator $\mathbf{L}$, and to the input forcing $\hat{\mathbf{f}} = (\hat{f}_u, \hat{f}_v, \hat{f}_w)^\mathrm{T}$ by operator $\mathbf{B}$. The system can be written in compact notation as follows:

$$\frac{\mathrm{d}\hat{\mathbf{q}}}{\mathrm{d}t} = \mathbf{L}\hat{\mathbf{q}} + \mathbf{B}\hat{\mathbf{f}}. \tag{7}$$

Equation (7) governs the dynamics of the perturbation variables, and we are interested in two particular cases: the temporal evolution of initial disturbances and the long-time response to external harmonic forcing.

2.2.1 Response to initial conditions

For a prescribed initial condition $\hat{\mathbf{q}}(0) = \hat{\mathbf{q}}_0$, the solution of Eq. (7) without any external forcing is given by

$$\hat{\mathbf{q}} = \exp(t\mathbf{L})\hat{\mathbf{q}}_0. \tag{8}$$

In order to study the stability of the system, we calculate the maximum energy amplification over a specified time interval and optimized over all initial conditions,

$$G(t) = \max_{\hat{\mathbf{q}}_0 \neq 0} \frac{||\hat{\mathbf{q}}(t)||_E^2}{||\hat{\mathbf{q}}_0||_E^2} = \max_{\hat{\mathbf{q}}_0 \neq 0} \frac{||\exp(t\mathbf{L})\hat{\mathbf{q}}_0||_E^2}{||\hat{\mathbf{q}}_0||_E^2} = ||\exp(t\mathbf{L})||_E^2, \tag{9}$$

where $|| \cdot ||_E$ is a norm that measures the kinetic energy of the perturbations [16]. The flow is asymptotically unstable when $G(t) \to \infty$ as $t \to \infty$, which will occur when at least one eigenvalue of $\mathbf{L}$ has a positive real part. On the counterpart, the flow is called asymptotically stable when $G(t) \to 0$ as $t \to \infty$.

2.2.2 Response to external harmonic forcing

For an external harmonic forcing $\hat{\mathbf{f}}(t) = \tilde{\mathbf{f}}\exp(-i\omega t)$, the particular solution to Eq. (7) is given by

$$\hat{\mathbf{q}} = (i\omega\mathbf{I} - \mathbf{L})^{-1}\mathbf{B}\hat{\mathbf{f}}. \tag{10}$$

This solution provides insight into the receptivity process, and for an asymptotically stable flow, it represents the long-time response of the system [6]. In order to study the receptivity of the system, we calculate the maximum energy amplification of the output optimized over all shapes of input forcing:

$$R(\omega) = \max_{\hat{\mathbf{f}} \neq 0} \frac{||\hat{\mathbf{q}}||_E}{||\hat{\mathbf{f}}||_E} = \max_{\hat{\mathbf{f}} \neq 0} \frac{||(i\omega\mathbf{I} - \mathbf{L})^{-1}\mathbf{B}\hat{\mathbf{f}}||_E^2}{||\hat{\mathbf{f}}||_E} = ||(i\omega\mathbf{I} - \mathbf{L})^{-1}\mathbf{B}||_E. \tag{11}$$

Therefore, the optimal response $R(\omega)$ is the resolvent norm [18].

2.3 Energy norm

A physically relevant quantity to measure growth is the kinetic energy of the perturbations. For a vector written in the normal velocity and normal vorticity formulation, the kinetic energy is calculated as follows [3]:

$$||\hat{\mathbf{q}}||_E^2 = \frac{1}{2k^2} \int_{-1}^{1} \left(|\mathcal{D}\hat{w}|^2 + k^2|\hat{w}|^2 + |\hat{\eta}|^2 \right) \mathrm{d}z = \hat{\mathbf{q}}^H \mathbf{Q}\hat{\mathbf{q}}, \tag{12}$$

where $\mathbf{Q}$ is the energy weight matrix that contains the appropriate weighting of the variables $(\hat{w}, \hat{\eta})^{\mathrm{T}}$ at the collocation points, as well as the integration weights between the channel walls. A Cholesky decomposition of $\mathbf{Q} = \mathbf{F}^H\mathbf{F}$ allows us to relate this norm to an equivalent standard (Euclidean) L_2-norm $||\hat{\mathbf{q}}||_E = ||\mathbf{F}\hat{\mathbf{q}}||_2$. The energy norm of a matrix $\mathbf{A}$ is easily derived using the definition of a vector-induced norm

$$||\mathbf{A}||_E = \max_{\hat{\mathbf{q}}} \frac{||\mathbf{A}\hat{\mathbf{q}}|_E}{||\hat{\mathbf{q}}||_E} = \max_{\hat{\mathbf{q}}} \frac{||\mathbf{FAF}^{-1}\mathbf{F}\hat{\mathbf{q}}||_2}{||\mathbf{F}\hat{\mathbf{q}}||_2} = ||\mathbf{FAF}^{-1}||_2. \tag{13}$$

Going back to Eqs. (9) and (11), we can rewrite the optimal growth rate $G(t)$ and the optimal response $R(\omega)$ as $L2$-norms:

$$G(t) = ||\mathbf{F} \exp(t\mathbf{L})\mathbf{F}^{-1}||_2^2, \tag{14a}$$

$$R(\omega) = ||\mathbf{F} (\mathrm{i}\omega\mathbf{I} - \mathbf{L})^{-1}\mathbf{B}\mathbf{F}^{-1}||_2. \tag{14b}$$

Before we can compute $G(t)$ and $R(\omega)$ from the above expressions, we have to perform a spectral decomposition of the operator $\mathbf{L} = \mathbf{V}\mathbf{\Lambda}\mathbf{V}^{-1}$. Here, $\mathbf{V}$ is the matrix whose columns are the eigenvectors of $\mathbf{L}$, and $\mathbf{\Lambda} = \mathrm{diag}(\lambda_1, \ldots, \lambda_{2N})$ is a diagonal matrix containing its eigenvalues, where $2N$ is the length of $\hat{\mathbf{q}}$. This way, the exponential and the resolvent of $\mathbf{L}$ can be easily calculated:

$$\exp(t\mathbf{L}) = \mathbf{V} \, \mathrm{diag}\left(\exp(t\lambda_1), \ldots, \exp(t\lambda_{2N})\right) \mathbf{V}^{-1}, \tag{15a}$$

$$(\mathrm{i}\omega\mathbf{I} - \mathbf{L})^{-1} = \mathbf{V} \, \mathrm{diag}\left(\frac{1}{\mathrm{i}\omega - \lambda_1}, \ldots, \frac{1}{\mathrm{i}\omega - \lambda_{2N}}\right) \mathbf{V}^{-1}. \tag{15b}$$

Using Eqs. (15), we can compute the matrices in Eqs. (14) and their Euclidean norm which is given by their largest singular value. Additionally, the principal right singular vector and principal left singular vector of each of these matrices correspond to the maximum amplification input and output disturbances, respectively, that is the optimal initial condition and the disturbance at time t for the exponential, and the optimal forcing and the response at a frequency ω for the resolvent. Computing the eigenvalues and eigenfunctions requires $O((2N)^3)$ arithmetic operations. To reduce the amount of computational work, we restrict our attention to the K least stable modes instead of all $2N$, thus requiring only $O(K^3)$ operations [13,18]. In this study, $N = 80$ and $K = 50$ are found to be enough for convergence of the computed results.

3 Results and discussion

3.1 Base flow

Our base flow considers the steady state in a swirl flow channel with an inlet angle $\theta_o = 8°$ and an aspect ratio $h/r_o = 0.02$, evaluated at a local radius r. Equations (1) allow us to calculate the local boundary layer thickness δ, the local flow angle θ_c at $z = 0$ (midplane), and the local Reynolds number Re, for different values of r, as shown in Fig. 2 [5].

Boundary layers in the swirl flow channel are merged ($\delta = 1$) for low Re_o, they separate over a certain value Re_o, and increments over that value result in thinning of the boundary layers, as shown in Fig. 2a. Figure 2b shows how the direction of the local flow at the midplane of the channel changes as Re_o increases. Starting from radial flow ($\theta_c = 90°$), the angle increases until we get tangential flow ($\theta_c = 0°$) when the boundary layers separate. Figure 2c shows the values of the local Reynolds number Re increasing as a function of the flow rate Reynolds number Re_o. When the boundary layers are merged, the local flow resembles a plane Poiseuille flow in the direction of θ_c and with a Reynolds number Re which is much lower than the critical value 5772 required for the flow to be asymptotically unstable [11]. As shown in Fig. 2, the overall behavior

of the base flow does not depend strongly on the local radius; therefore, we arbitrarily select $r = 0.6r_o$ as a representative local radius for the fluid dynamics in a swirl flow channel. Although our conclusions in this study are not affected by this particular value, we consider that a global stability analysis is a logical next step for future work.

3.2 Stability and receptivity

Optimal growth $G(t)$ and optimal response $R(\omega)$ are calculated for flow rate Reynolds numbers Re_o between 0.1 and 2. In order to study the influence of the wavevector, instead of using its radial and azimuthal components α and β, we use its magnitude $k = \sqrt{\alpha^2 + \beta^2}$ and the waveangle defined as $\theta_k = \arctan(\alpha/\beta) - \theta_c$. In this notation, an angle $\theta_k = 0°$ represents a wave propagating in the direction of flow in the midplane of the channel (aligned with θ_c), which we refer to as the streamwise direction. Therefore, we refer to $\theta_k = 90°$ as the crossflow direction, and it represents a wave direction normal to the flow at $z = 0$. This formulation allows for an easier physical interpretation of the results, because the streamwise and crossflow directions of the base flow change with Re_o, as shown in Fig. 2b.

Figure 3 shows the different behaviors of $G(t)$ and $R(\omega)$ that can be observed for different k, θ_k, and Re_o. Flow may be asymptotically unstable and therefore have unbounded energy growth, it may be stable but present some transient growth, or it can present monotonic energy decay, as shown in Fig. 3a. The flow is found to be highly receptive to stationary crossflow waves, as shown in Fig. 3b, and mildly receptive to streamwise traveling waves with two different frequencies, as shown by the two peaks in Fig. 3c.

For asymptotically stable flows, we calculate the maximum values of $G(t)$ and $R(\omega)$ and denote them G_{max} and R_{max}, respectively. The dependence of G_{max} and R_{max} on the total wavenumber k and the waveangle θ_k for $Re_o = 0.8$ is shown in Fig. 4. Maximum growth is observed for $k = 2.12$, and the maximum response is
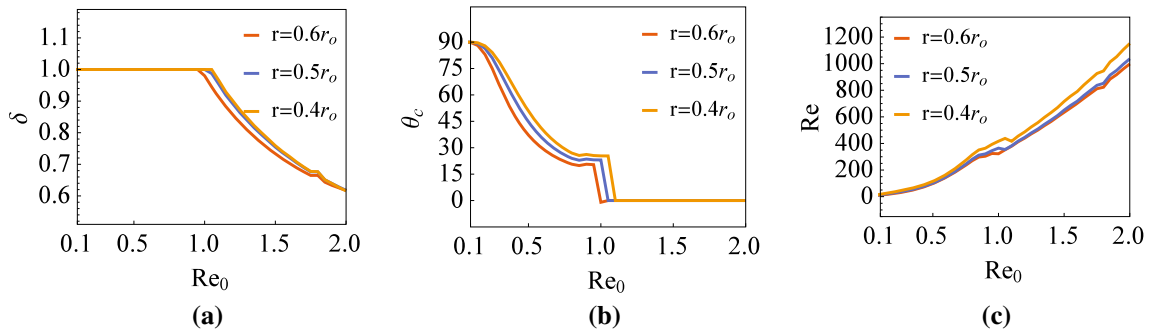

Fig. 2 Base flow variables as a function of the flow rate Reynolds number Re_o at different local radii $r/r_o = 0.4, 0.5$, and 0.6. **a** Boundary layer thickness δ. **b** Flow angle at the midplane of the channel θ_c, measured starting from the tangential direction. **c** Local Reynolds number Re, based on the half-height of the channel and the streamwise velocity component at $z = 0$ (midplane)
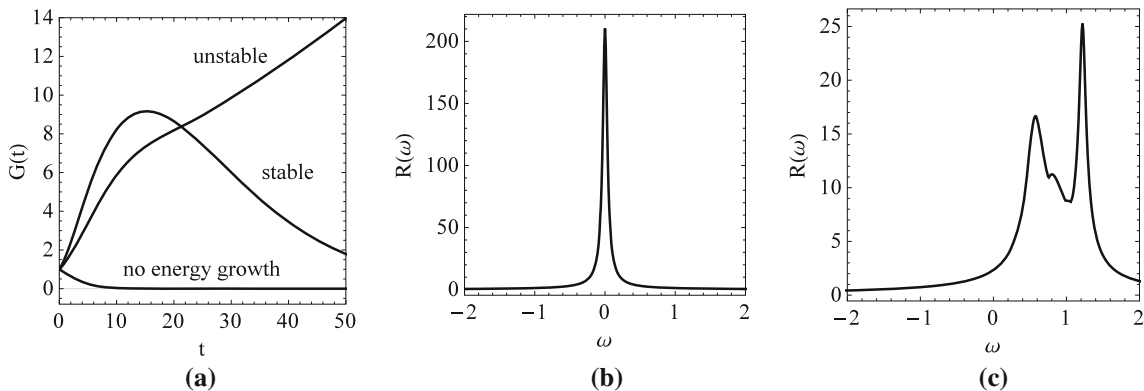

Fig. 3 **a** Optimal growth $G(t)$ in the crossflow direction. Curves labeled unstable for $Re_o = 1.07$ and $k = 0.75$, stable for $Re_o = 0.62$ and $k = 2.25$, and no energy growth for $Re_o = 0.30$ and $k = 2.25$. **b**, **c** Optimal response $R(\omega)$ for $Re_o = 0.8$ and $k = 1.25$. **b** Crossflow direction $\theta_k = 90°$. **c** Streamwise direction $\theta_k = 0°$
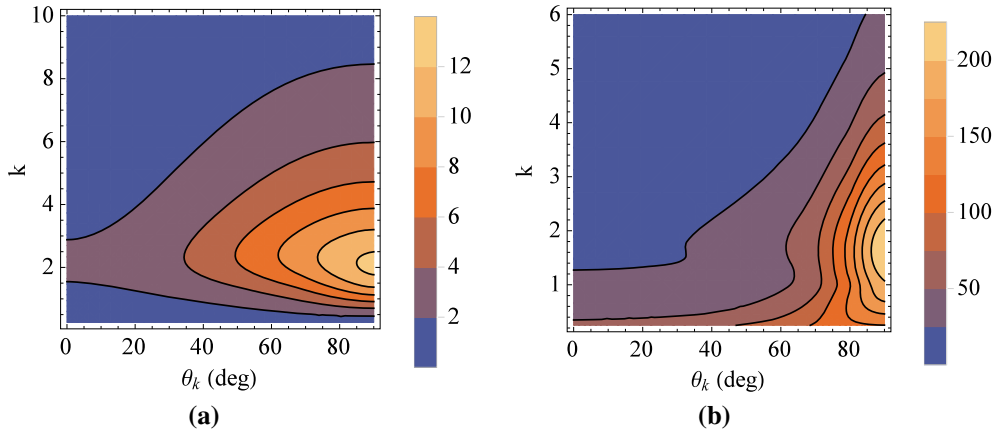
Fig. 4 Contours of **a** maximum transient amplification $G_{\max}$ and **b** maximum frequency response $R_{\max}$ as a function of the total wavenumber k and the waveangle θ_k for $Re_{\mathrm{o}} = 0.8$

obtained for $k = 1.63$, both along the crossflow direction $\theta_k = 90°$, where the base flow velocity profiles are most inflectional.

Figure 5 shows vector fields of relevant disturbances in the y–z plane, where y is the coordinate along the wave direction. The disturbance that achieves the largest transient amplification, i.e., the optimal initial condition, corresponds to streamwise vortices, as shown in Fig. 5a for $Re_{\mathrm{o}} = 0.8$. Similarly to plane Poiseuille flow, Fig. 5b shows that these vortices change little as time evolves; however, high energy streamwise streaks will form due to the lift-up effect. The most responsive forcing and the most receptive disturbance, i.e., the optimal forcing and the optimal response, are shown in Fig. 5c, d for $Re_{\mathrm{o}} = 0.8$, and the leading eigenmode for unstable flow at $Re_{\mathrm{o}} = 1.07$ is shown in Fig. 5e.

The Re_{o} dependence of $G_{\max}$ in the crossflow direction and the neutral curve for asymptotic stability are shown in Fig. 6. Two important values for the flow rate Reynolds numbers are calculated: $Re_{\mathrm{o}}^{E} = 0.36$, below which there is no energy growth of disturbances, and $Re_{\mathrm{o}}^{c} = 0.91$ that delimits the onset of asymptotic instability where there is unbounded energy growth. Between these values, perturbations experience transient growth followed by asymptotic decay, where the kinetic energy is amplified up to $O(10)$, as shown in Fig. 6. For plane Poiseuille flow, transient growth plays an important role in the transition process, whereas for the swirl flow channel, we find very small transient growth. This suggests that the mechanism for transition is the change in the shape of the velocity profile due to rotational effects (crossflow instability). It is worth noting that Ruiz and Carey in Ref. [15] observed that their experimental results deviated from laminar behavior for flow rates over 190 ml/min, which corresponds to $Re_{\mathrm{o}} = 0.86$ according to our definition of the flow rate Reynolds number. Therefore, we find reasonable agreement between experimental observations and predictions from our simplified analysis. The critical value for the Reynolds number, Re_{o}^{c}, is also useful to determine bounds for the validity of assumptions and models of the flow inside this type of channel.

The maximum response of the system $R_{\max}$ increases with the flow rate Reynolds number, and when approaching Re_{o}^{c}, the forcing energy amplification is of $O(100)$. The forcing frequency and the waveangle that give $R_{\max}$ are $\omega = 0$ and $\theta_k = 90°$, and do not change with Re_{o}. Nevertheless, the direction of the base flow at the midplane of the channel is affected. Consequently, when increasing Re_{o}, crossflow waves manifest as spirals of decreasing number of arms. The onset of asymptotic instability coincides with the separation of the boundary layers and the appearance of velocity profiles that are most inflectional in the radial direction. The fastest growing mode corresponds to axisymmetric circular waves that travel radially inward, and its structure is shown in Fig. 5e. The characteristics of the forcing or disturbances that are largely amplified by the flow are important for the design and operation of technological devices. A large response should be avoided to ensure the safe operation of a parallel-disk turbine, but it may be sought to promote mixing in a swirl flow channel heat sink.
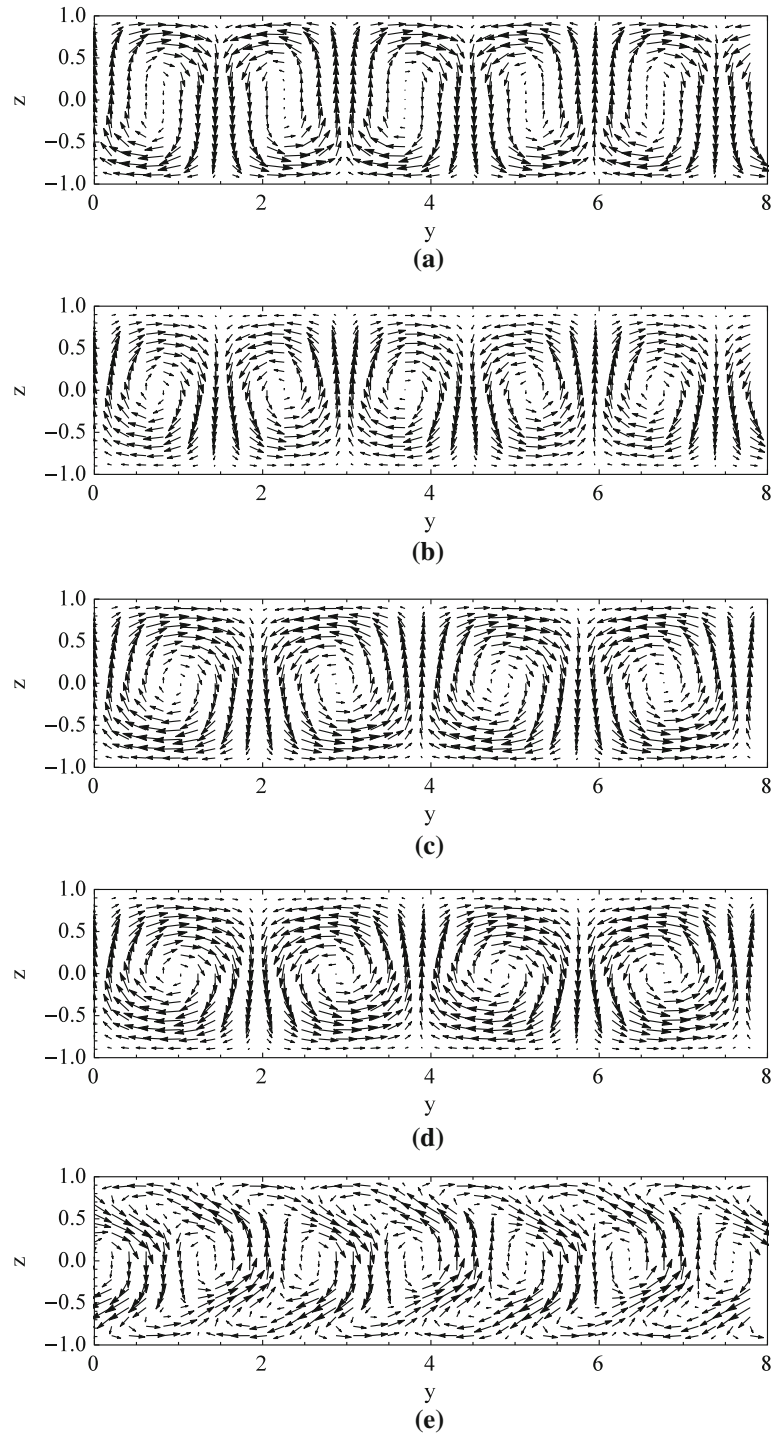
(a)

(b)

(c)

(d)

(e)

Fig. 5 Disturbance vector fields for $\theta_k = 90°$ in the y–z plane, where y is the coordinate along the wave direction. **a**, **b** Optimal initial condition and its structure after maximum transient amplification for $Re_o = 0.8$ and $k = 2.12$. **c**, **d** Optimal forcing and response for $Re_o = 0.8$ and $k = 1.63$. **e** Most unstable eigenmode for $Re_o = 1.07$ and $k = 2.52$
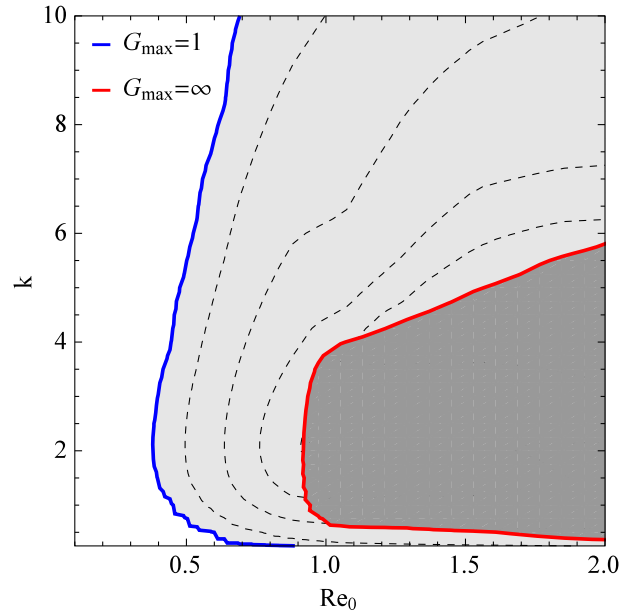
Fig. 6 Contours of $G_{\max}(k, 90°, Re_o)$. Three regions can be distinguished: asymptotic instability (dark gray), asymptotic decay with transient growth (light gray), and asymptotic decay without energy growth (white). Dashed contour levels, from left to right, $G_{\max} = 2, 5, 10, 15$

4 Conclusions

This study provides numerical solutions for the energy growth of initial disturbances and the response to external harmonic forcing in a swirl flow channel. The methodology is emphasized with a clear presentation of the simplifications that are used. Linearized perturbation equations are obtained using the local and parallel flow approximations based on order of magnitude arguments. The result is equivalent to the Orr-Sommerfeld and Squire system for a three-dimensional boundary layer.

The effect of the flow rate Reynolds number on the base flow is presented. When Re_o increases, the flow direction on the channel midplane changes gradually from radial to azimuthal and eventually boundary layers separate. Results for the stability analysis show that there is no energy growth if the Reynolds number is less than $Re_o^E = 0.36$, and the flow becomes asymptotically unstable over $Re_o^c = 0.91$ which coincides with the separation of the boundary layers. As opposed to plane Poiseuille flow, there is very little transient growth between Re_o^E and Re_o^c, with an energy amplification only up to $O(10)$. This suggests that the mechanism for transition to turbulence is the crossflow instability that occurs due to the change in the shape of the base flow velocity profiles over Re_o^c. Our results are able to predict transition, as they present reasonable agreement with experimental observations made by other authors in Ref. [15].

The particular solution to the harmonically driven problem, i.e., the receptivity analysis, shows a large response of the fluid system to external disturbances for subcritical Reynolds numbers, with energy amplification up to $O(100)$. As Re_o increases, the flow becomes increasingly receptive to stationary spiral crossflow waves of decreasing number of arms. For asymptotically unstable flow, the fastest growing mode corresponds to axisymmetric circular waves that travel radially inward, which is the direction of the most inflectional velocity profile. Future work considers including the heat equation and studying the componentwise frequency response to determine heat transfer enhancement strategies in a swirl flow channel heat sink.

Stability and receptivity of the flow are not only of fundamental interest, but are also relevant to modeling, design, operation, and control of parallel-disk turbines and swirl flow channel heat sinks. The methodology presented is particularly useful for early design stages due to its ease of implementation and low computational cost, which allows an exploration of geometric parameters and operating conditions.

References

1. Do, Y., Lopez, J.M., Marques, F.: Optimal harmonic response in a confined Bödewadt boundary layer flow. Phys. Rev. E **82**(3), 036301 (2010)
2. Gregory, N., Stuart, J.T., Walker, W.S.: On the stability of three-dimensional boundary layers with application to the flow due to a rotating disk. Philos. Trans. R. Soc. Lond. **248**(943), 155–199 (1955)
3. Gustavsson, L.H.: Excitation of direct resonances in plane Poiseuille flow. Stud. Appl. Math. **75**(3), 227–248 (1986)
4. Herrmann-Priesnitz, B., Calderón-Muñoz, W.R., Salas, E.A., Vargas-Uscategui, A., Duarte-Mermoud, M.A., Torres, D.A.: Hydrodynamic structure of the boundary layers in a rotating cylindrical cavity with radial inflow. Phys. Fluids **28**(3), 033601 (2016)
5. Herrmann-Priesnitz, B., Calderón-Muñoz, W.R., Valencia, A., Soto, R.: Thermal design exploration of a swirl flow microchannel heat sink for high heat flux applications based on numerical simulations. Appl. Therm. Eng. **109**, 22–34 (2016)
6. Jovanović, M.R., Bamieh, B.: Componentwise energy amplification in channel flows. J. Fluid Mech. **534**, 145–183 (2005)
7. Krishnan, V.G., Romanin, V., Carey, V.P., Maharbiz, M.M.: Design and scaling of microscale Tesla turbines. J. Micromech. Microeng. **23**(12), 125001 (2013)
8. Lingwood, R.J.: Absolute instability of the boundary layer on a rotating disk. J. Fluid Mech. **299**, 17–33 (1995)
9. Lopez, J.M., Marques, F., Rubio, A.M., Avila, M.: Crossflow instability of finite Bödewadt flows: transients and spiral waves. Phys. Fluids **21**(11), 114107 (2009)
10. Malik, M.R.: The neutral curve for stationary disturbances in rotating-disk flow. J. Fluid Mech. **164**, 275–287 (1986)
11. Orszag, S.A.: Accurate solution of the Orr-Sommerfeld stability equation. J. Fluid Mech. **50**(4), 689–703 (1971)
12. Pfenniger, A., Vogel, R., Koch, V.M., Jonsson, M.: Performance analysis of a miniature turbine generator for intracorporeal energy harvesting. Artif. Organs **38**(5), E68 (2014)
13. Reddy, S.C., Henningson, D.S.: Energy growth in viscous channel flows. J. Fluid Mech. **252**, 209–238 (1993)
14. Ruiz, M., Carey, V.P.: Prediction of single phase heat and momentum transport in a spiraling radial inflow microchannel heat sink. ASME. Paper No. HT2012-58328 (2012)
15. Ruiz, M., Carey, V.P.: Experimental study of single phase heat transfer and pressure loss in a spiraling radial inflow microchannel heat sink. J. Heat Transfer **137**(7), 071702 (2015)
16. Schmid, P.J.: Nonmodal stability theory. Annu. Rev. Fluid Mech. **39**(1), 129–162 (2007)
17. Schmid, P.J., Brandt, L.: Analysis of fluid systems: stability, receptivity, sensitivity. Appl. Mech. Rev. **66**(2), 024803 (2013)
18. Schmid, P.J., Henningson, D.S.: Stability and Transition in Shear Flows. Springer, New York (2001)
19. Sengupta, S., Guha, A.: The fluid dynamics of symmetry and momentum transfer in microchannels within co-rotating discs with discrete multiple inflows. Phys. Fluids **29**(9), 093604 (2017)
20. Serre, E., del Arco, E.C., Bontoux, P.: Annular and spiral patterns in flows between rotating and stationary discs. J. Fluid Mech. **434**, 65–100 (2001)
21. Trefethen, L.N., Trefethen, A.E., Reddy, S.C., Driscoll, T.A.: Hydrodynamic stability without eigenvalues. Science **261**(5121), 578–584 (1993)